Front. Phys. 13(3), 138109 (2018)
https://doi.org/10.1007/s11467-018-0782-2

RESEARCH ARTICLE

Two-dimensional aluminum monoxide nanosheets: A computational study

Shiru Lin[1], **Yanchao Wang**[2], **Zhongfang Chen**[1,†]

[1] *Department of Chemistry, University of Puerto Rico, Rio Piedras Campus, San Juan, PR 00931, USA*
[2] *State Key Lab of Superhard Materials, Jilin University, Changchun 130012, China*
Corresponding author. E-mail: [†] *zhongfangchen@gmail.com*
Received March 13, 2018; accepted March 27, 2018

By means of density functional theory (DFT) computations and particle-swarm optimization (PSO) structure searches, we herein predict five low-lying energy structures of two-dimensional (2D) aluminum monoxide (AlO) nanosheets. Their high cohesive energy, absence of imaginary phonon dispersion, and good thermal stability make them feasible targets for experimental realization. These monolayers exhibit diverse structural topologies, for instance, *PmA*- and *Pmm*-AlO possess buckled four- and six-membered AlO rings, whereas *P*62-, *PmB*-, and *P*6*m*-AlO have pores of varied sizes. Interestingly, the most energetically preferred monolayers, *PmA*- and *Pmm*-AlO, feature wide band gaps (2.45 and 5.13 eV, respectively), which are promising for green and blue light-emitting devices (LEDs) and photodetectors.

Keywords 2D materials, density functional calculations, particle swarm optimization, wide-band-gap semiconductor

PACS numbers 73.21.-b, 73.22.-f

1 Introduction

The successful experimental realization of graphene [1] and the discovery of its exceptional electronic and transport properties [2–6] inspired tremendous efforts to investigate other two-dimensional (2D) materials [7–14]. Until now, numerous elemental 2D materials, such as group-IV silicene [15–21], germanene [22–27], and stanene [28–32]; and group-V phosphorene [33–39], arsenene [40–43], and antimonene [41–47], have been experimentally fabricated and/or theoretically studied. Aluminene, as an important member of group-III monolayers, has also been explored theoretically, and buckled aluminene (*P*-3m1 point group) was reported to have the lowest energy and a metallic nature [48, 49].

Aluminum can be easily oxidized, and aluminum oxides have been commonly utilized in different areas. There are three aluminum oxide compounds: aluminum monoxide (AlO), dialuminum oxide (Al_2O), and dialuminum trioxide (Al_2O_3). Both AlO and Al_2O exist in the gaseous state [50, 51] with a linear structure [52, 53]. The most commonly known aluminum oxide is Al_2O_3, which is widely used as solid electrolytes [54] and catalysts [55]. Aluminum and oxygen are two of the most abundant elements in the earth, however, little work has focused on 2D aluminum oxide materials. Recently, Song *et al.* [56] theoretically designed a planar Al_2O_3 layered material with a direct band gap of 5.99 eV. In its honeycomb lattice, aluminum atoms are at the vertices of hexagons and linearly connected by the oxygen atoms. Apparently, different oxygen concentrations in aluminum oxides can lead to various stable 2D nanostructures, and these nanosheets may present rather unique properties. Thus, it is interesting to explore the geometric structures and electronic properties of 2D aluminum oxide nanosheets with other stoichiometries.

In this work, by means of density functional theory (DFT) computations and global-minimum structure searches, we theoretically predicted the five low-lying-energy 2D aluminum monoxide (AlO) nanosheets. These newly predicted monolayers have varied structural topologies and cover a wide range of band gaps (from 1.76 to 6.51 eV). Their highly positive cohesive energies, absence of imaginary phonon dispersion, and good thermal stability indicate the feasibility of their experimental realization. In particular, the two lowest energy configurations, *PmA*- and *Pmm*-AlO, which feature wide band

*Special Topic: Inorganic Two-Dimensional Nanomaterials (Eds. Changzheng Wu & Xiaojun Wu).

Frontiers of Physics

gaps (2.45 and 5.13 eV, respectively), are promising for many applications and are highly recommended as experimental targets.

2 Computation methods

Our DFT computations were performed using ultrasoft pseudopotentials, as implemented in the CASTEP code [57]. The suitability of the ultrasoft pseudopotential for the systems under study was validated (Figs. A1 and A2, Table A1). The electron exchange-correlation functional was treated using generalized gradient approximation (GGA) in the form proposed by Perdew, Burke, and Ernzerhof (PBE). The energy cutoff was set at 500 eV, the convergence tolerance was 10^{-5} eV, and the vacuum spaces are more than 15 Å, so that the interactions between adjacent layers can be ignored. The Monkhost–Pack k points were set as $7\times3\times1$, $5\times6\times1$, $4\times4\times1$, $2\times6\times1$, and $4\times4\times1$ for geometry optimizations and self-consistent calculations of the five monolayers under investigation. We carried out both spin-polarized and spin-unpolarized computations and ensured that all the AlO monolayers have no magnetism. To evaluate the dynamic stability of the AlO monolayers, we computed the phonon dispersions using $2\times2\times1$ supercells and 10^{-6} eV convergence tolerances.

We also performed *ab initio* molecular dynamics (AIMD) simulations using a Nosé–Hoover thermostat in NVT canonical ensemble to evaluate the thermal stability of the AlO monolayers. The $2\times2\times1$ AlO supercells ($3\times2\times1$ supercell for *Pmm*-AlO) were simulated at different temperatures of 300, 500, and 1000 K, and each simulation lasted for 10 ps with a time step of 2.0 fs.

Because the PBE functional tends to underestimate the band gap values and with recent studies demonstrating that the GLLB-sc potential as implemented in GPAW code [58] enables improved band gap calculations by including the derivative discontinuity absent in PBE [59–61], we also carried out band-gap computations using the GLLB-sc potential to obtain more accurate values.

The particle-swarm optimization (PSO) method, as implemented in the CALYPSO code [62], was used to search for stable 2D AlO monolayers. The optimizations were performed by the CASTEP code using the PBE functional. In our calculations, the population size was set at 30, and the number of generations 50. Unit cells containing 1–6 aluminum atoms and the same number of oxygen atoms were considered. The CALYPSO search helped us to find the low-lying energy structures of AlO monolayers in the 2D space.

3 Results and discussion

3.1 Geometric structures

Our CALYPSO search resulted in five low-lying-energy 2D aluminum oxide nanosheets (Fig. 1), which are denoted by the first three letters/numbers of their symmetries, i.e., *PmA*-, *Pmm*-, *P*62-, *PmB*- and *P*6*m*- AlO (two structures with *Pm* symmetry are differentiated by A and B). These monolayers exhibit diverse structural topologies, as indicated by their key structural parameters (Table 1) and optimized geometries (Fig. 1), and can be divided into two groups: the buckled *PmA*- and *Pmm*-AlO, and the planar and porous *P*62-, *PmB*-, and *P*6*m*-AlO monolayers.

Both buckled monolayers, *PmA*- and *Pmm*-AlO, consist of six- and four-membered rings. They differ most in that only *PmA*-AlO has lines of AlO-interlaced six-membered Al_3O_3 rings, leading to a different buckled structure with thicknesses (h) of 0.152 and 0.076 Å for *PmA*- and *Pmm*-AlO, respectively. In comparison, the remaining three AlO monolayers are planar, among which *P*62 and *PmB* have 10- and 10/11/9-membered rings with pore sizes of 4.34 and 4.86/4.72/5.23 Å, respectively, and *P*6*m* possesses fairly large 18-memberred rings with pores 8.85 Å in diameter.

A significant difference between the abovementioned two groups is that the buckled structures (*PmA*-AlO and *Pmm*-AlO) contain tetra-, penta-, and hexa-coordinated aluminum atoms as well as tri-coordinated oxygen atoms, whereas the planar porous ones (*P*62-, *PmB*-, and *P*6*m*-AlO) merely contain tri-coordinated aluminum atoms and bi-coordinated oxygen atoms (Fig. 1). Thus, it is the larger coordinate numbers and greater number of chemical bonds that make the *PmA*- and *Pmm*-AlO

Table 1 Key structural parameters (lattice parameters, Al-O and Al-Al bond lengths), cohesive energies (E_c), and band gaps (E_g) of AlO monolayers.

Structure	*PmA*-AlO	*Pmm*-AlO	*P*62-AlO	*PmB*-AlO	*P*6*m*-AlO
Symmetry	*Pm*	*Pmmn*	*P*-62*m*	*Pm*	*P*6/*mmm*
Lattice parameters (Å)	$a=7.25$; $b=6.00$	$a=3.62$; $b=9.67$	$a=b=9.12$	$a=14.42$; $b=5.23$	$a=b=10.55$
Al-O (Å)	1.70–1.94	1.77; 1.91	1.68	1.68; 1.69	1.72
Al-Al (Å)	2.55–2.72	2.79; 2.76	2.54	2.60	2.56
E_c (eV/atom)	5.61	5.55	5.39	5.37	5.36
E_g (PBE) (eV)	0.81	2.42	1.56	0.28	3.53
E_g (GLLB-sc) (eV)	2.45	5.13	3.54	1.76	6.51

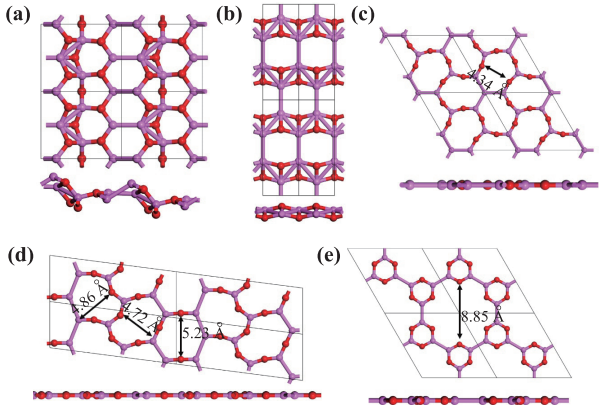

Fig. 1 Top and side views of **(a)** *PmA*-, **(b)** *Pmm*-, **(c)** *P*62-, **(d)** *PmB*-, and **(e)** *P*6*m*-AlO monolayers. The red and rose-carmine atoms represent O and Al atoms, respectively. For clarity, $(2 \times 2 \times 1)$ supercells are presented here.

monolayers energetically more favorable than the other configurations.

3.2 Thermodynamic, dynamic, and thermal stability

The stability of a material is highly important for its experimental realization and future applications. Thus, we carefully examined the thermodynamic, dynamic, and thermal stabilities of these AlO monolayers. First, we examined their thermodynamic stabilities by computing their cohesive energies (E_c), defined as

$$E_c = nE_{Al} + nE_O - E_{AlO}/2n,$$

where n stands for the number of aluminum/oxygen atoms in a unit cell (*Pmm*-AlO unit cell is composed of four aluminum atoms and four oxygen atoms, and the others contain six aluminum atoms and six oxygen atoms); E_{Al}, E_O, and E_{AlO} are the total energies of the single atoms and material unit cell. According to our definition, the structure with a more positive cohesive energy (lower system energy) is thermodynamically more favorable. The computed cohesive energies of these newly predicted AlO monolayers are all highly positive, and are 5.61, 5.55, 5.39, 5.37, 5.36 eV/atom (Table 1). These cohesive energies are smaller than that of 2D-Al_2O_3 (5.97 eV/atom [56]), but higher than that of buckled-aluminene (3.18 eV/atom) at the same theoretical level, indicating the importance of strong Al–O covalent bonds for the stability of aluminum oxides. Note that *PmA*-AlO has the highest average cohesive energy (5.61 eV/atom), followed by *Pmm*-AlO, the other buckled nanosheets, which is 0.06 eV/atom higher in sys-

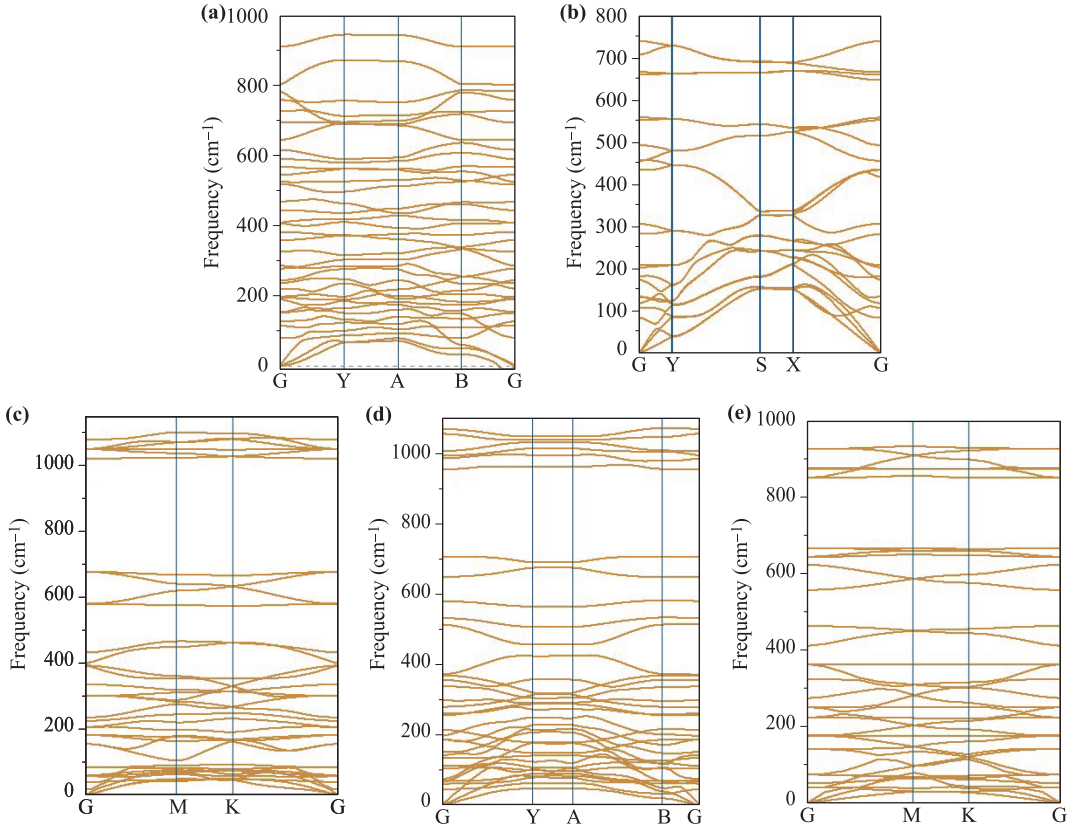

Fig. 2 Phonon dispersions of **(a)** *PmA*-, **(b)** *Pmm*-, **(c)** *P*62-, **(d)** *PmB*-, and **(e)** *P*6*m*-AlO monolayers.

tem energy. However, the three planar and porous structures are 0.22–0.25 eV/atom higher in system energies. Thus, *PmA*-AlO is the global minimum structure in 2D space, and has a better chance for experimental realization, whereas the others are metastable but also highly feasible experimentally.

Secondly, we investigated the dynamic stabilities of these AlO monolayers by computing their phonon dispersions. Note that no significant imaginary frequency was found. Thus, the phonon dispersions confirm that these five 2D AlO nanosheets are dynamically stable and represent the local minima.

Thirdly, we evaluated the thermal stability of the aluminum monoxide nanosheets by AIMD simulations (Fig. 3). At room temperature (300 K), all of the five AlO monolayers effectively maintain their geometries; *Pmm*-, *P*62-, and *P*6*m*-AlO nanosheets can preserve their structures at temperatures of up to 1000 K, indicating their outstanding stabilities at extremely high temperatures.

In general, the good thermodynamic, dynamic, and thermal stabilities, as revealed by the computed cohesive energies, phonon dispersions, AIMD simulations, and PSO global minimum search, strongly indicate the high feasibility for experimental realization of these predicted aluminum monoxide nanosheets.

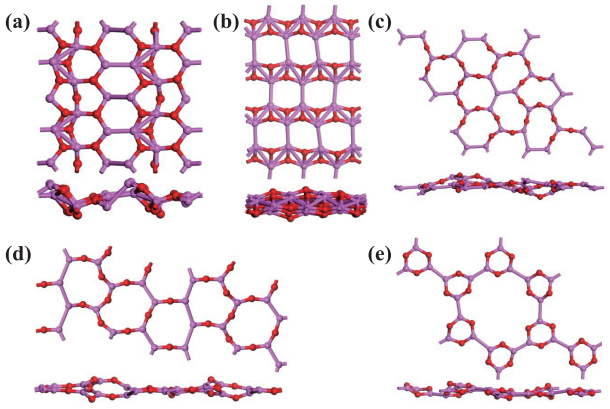

Fig. 3 Snapshots of **(a)** *PmA*-, **(b)** *Pmm*-, **(c)** *P*62-, **(d)** *PmB*-, and **(e)** *P*6*m*-AlO equilibrium structures at (a) 300 K, (b) 1000 K, (c) 1000 K, (d) 300 K and (e) 1000 K at the end of 10 *ps* AIMD simulations.

3.3 Electronic properties

To study the electronic properties of 2D AlO monolayers, we first computed their band structures as well as the partial density of states (PDOS) at the PBE level of theory (Fig. 4). No band line across the Fermi level is available in any of the computed band structures; thus, all of these AlO monolayers are semiconducting. Nevertheless, these AlO monolayers possess diverse band-gap types and values (Table 1). *Pmm*-AlO, *P*62-AlO, and *PmB*-AlO have direct band gaps at point G, and their band gaps are theoretically 2.42, 1.56, and 0.28 eV at the PBE level, respectively, whereas *PmA*-AlO and *P*6*m*-AlO have indirect band gaps of 0.81 and 3.53 eV, respectively, based on the PBE functional. The conduction band minimum (CBM) of *PmA*-AlO is at point A (0.5, 0.5, 0), and the valence band maximum (VBM) is

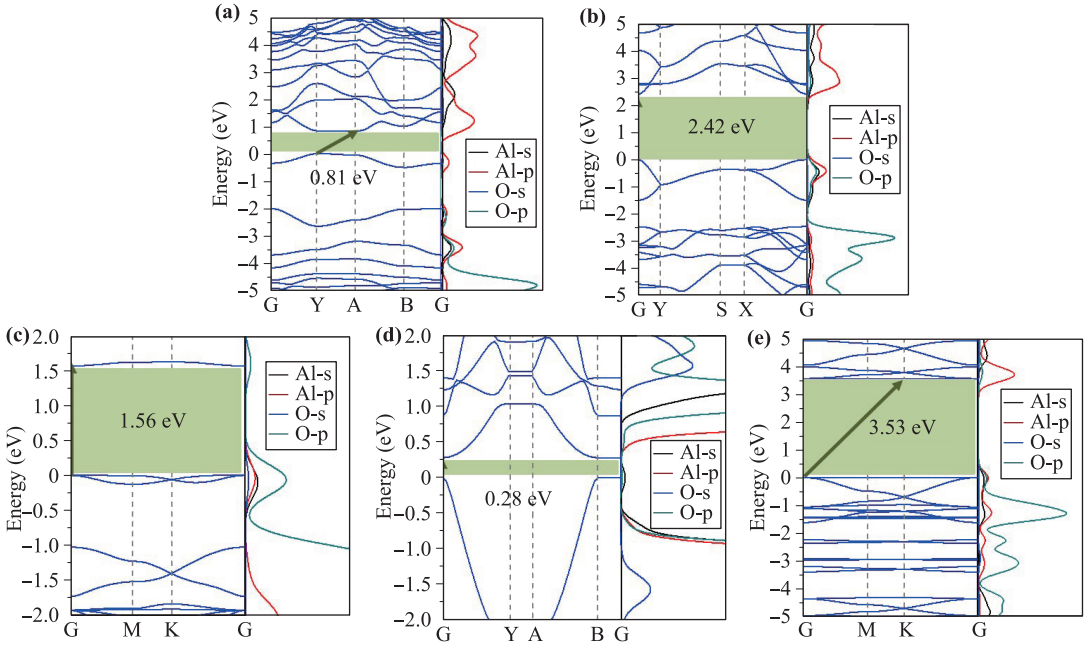

Fig. 4 Band structures of **(a)** *PmA*-, **(b)** *Pmm*-, **(c)** *P*62-, **(d)** *PmB*-, and **(e)** *P*6*m*-AlO monolayers (by PBE functional).

at point Y (0, 0.5, 0). The CBM of *P6m*-AlO is at point K (0.333, 0.333, 0) and its VBM is at point G.

We then carefully analyzed the PDOS plots to check the orbital contributions of the bands close to the Fermi level. For the lowest-energy AlO monolayer, i.e., *PmA*-AlO, its VBM and CBM are mainly provided by the *p* orbitals of the aluminum atoms, and their electron densities are mostly contributed by the *p* orbitals of the aluminum atoms along the Al_4O_2 rings [Figs. 5(a) and (b)]. The VBM of *Pmm*-AlO, the second-lowest-energy AlO monolayer, is contributed by the hybridization of the oxygen *p* orbitals and aluminum *s* and *p* orbitals, and its CBM can be mainly attributed to the *p* orbitals of the aluminum atoms [Figs. 5(c) and (d)].

We also computed the band gap using the GLLB-sc functional, whose good performance in predicting band gap values has been validated [59]. The band gaps of the *PmA*-, *Pmm*, *P*62-, *PmB*-, and *P6m*-AlO monolayers are 2.45, 5.13, 3.54, 1.76, and 6.51 eV, respectively, covering a wide range of values.

Interestingly, the two lowest-energy AlO monolayers, which are expected to be dominant owing to their much better thermodynamic stabilities both feature wide band gaps larger than 2.0 eV [41, 63–65]. Note that wide-band-gap semiconductors are essential to realize devices for high-voltage [66], high-power, and high-temperature operations [67, 68], but have not been developed thoroughly owing to the scarcity of such materials. Similar to h-BN [69, 70], our newly predicted, experimentally feasible 2D *Pmm*- and *PmA*-AlO monolayers are wide-band-gap semiconductors, and are thus very promising for applications, among others, in high-power ultrathin electronics, green and blue LEDs, blue-violet laser diodes, and photodetectors [71–73].

4 Conclusion

We theoretically investigated the structure, stability and electronic properties of five low-lying energy 2D aluminum monoxide nanosheets by means of PSO searches and systematic DFT computations. Among the five structures under investigation, the buckled *PmA*-AlO has the lowest energy, closely followed by the buckled structure, *Pmm*-AlO, whereas the other three structures, *P*62-, *PmB*-, and *P6m*-AlO, are planar and have pores with different sizes (4.34–8.85-Å diameters). These monolayers are semiconducting with indirect or direct band gaps ranging from 1.76 to 6.51 eV (GLLB-sc functional). All these monolayers are thermodynamically, dynamically, and thermally stable, as indicated by their rather high cohesive energies, absence of imaginary phonon dispersions, and well-preserved geometric structures in high temperatures, which strongly indicate their feasibility for experimental realizations. In particular, the two lowest-energy AlO monolayers, which are expected to be synthesized with a higher probability, are both wide-band-gap semiconductors, and therefore have enormous potential for use in devices including high-power ultrathin electronics, green and blue LEDs, blue-violet laser diodes, and photodetectors. We hope that our newly predicted 2D AlO nanosheets will inspire more efforts on 2D main-group oxide materials with unusual structural and electronic properties.

Acknowledgements This work was supported by the National Science Foundation-Centers of Research Excellence in Science and Technology (NSF-CREST Center) for Innovation, Research and Education in Environmental Nanotechnology (CIRE2N) (Grant No. HRD-1736093) and NASA (Grant No. 17-EPSCoRProp-0032).

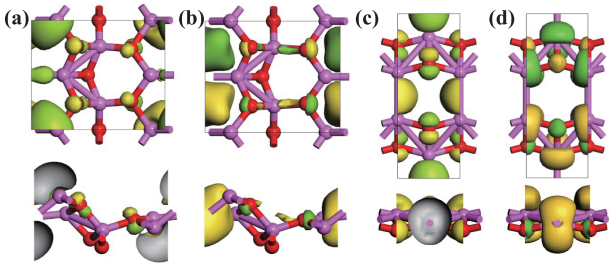

Fig. 5 Electron density distributions (isosurface = 0.04 a.u.): **(a)** VBM and **(b)** CBM of *PmA*-AlO monolayer; **(c)** VBM and **(d)** CBM of *Pmm*-AlO monolayer.

Appendix A Supplementary information

Optimized geometric structure and predicted band structure of *PmA*-AlO and *Pmm*-AlO nanosheets using norm-conserving pseudopotential at PBE level of theory, and the comparison of the computational results using norm-conserving pseudopotential and ultra-soft pseudopotential.

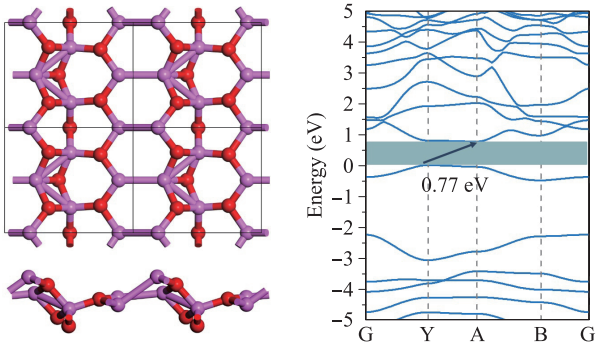

Fig. A1 Optimized structure (left) and band structure (right) of *PmA*-AlO nanosheet using norm-conserving pseudopotential at PBE function of theory.

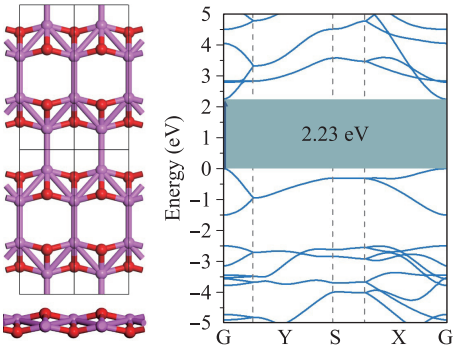

Fig. A2 Optimized structure (left) and band structure (right) of *Pmm*-AlO nanosheet using norm-conserving pseudopotential at PBE function of theory.

Table A1 Optimized Al-O and Al-Al bond lengths and band gaps (E_g, eV) of *PmA*- and *Pmm*-AlO nanosheets using norm-conserving pseudopotential at PBE function of theory, and the differences of bond lengths and band gaps of them using ultrasoft pseudopotential and norm-sorving potential.

Structure	*PmA*-AlO	*Pmm*-AlO
Al-O	1.66–1.83	1.77; 1.91
Δ_{Max} of Al-O bonds (Å)	0.11	~ 0
Al-Al (Å)	2.50–2.64	2.79; 2.76
Δ_{Max} of Al-Al bonds (Å)	0.08	~ 0
E_g (PBE) (eV)	0.77	2.23
ΔE_g (eV)	0.04	0.19

References

1. K. S. Novoselov, A. K. Geim, S. V. Morozov, D. Jiang, Y. Zhang, S. V. Dubonos, I. V. Grigorieva, and A. A. Firsov, Electric field effect in atomically thin carbon films, *Science* 306(5696), 666 (2004)
2. Y. Zhang, Y. W. Tan, H. L. Stormer, and P. Kim, Experimental observation of the quantum Hall effect and Berry's phase in graphene, *Nature* 438(7065), 201 (2005)
3. C. L. Kane and E. J. Mele, Quantum spin Hall effect in graphene, *Phys. Rev. Lett.* 95(22), 226801 (2005)
4. K. S. Novoselov, A. K. Geim, S. Morozov, D. Jiang, M. Katsnelson, I. Grigorieva, S. Dubonos, and A. Firsov, Two-dimensional gas of massless Dirac fermions in graphene, *Nature* 438(7065), 197 (2005)
5. S. V. Morozov, K. S. Novoselov, M. I. Katsnelson, F. Schedin, D. C. Elias, J. A. Jaszczak, and A. K. Geim, Giant intrinsic carrier mobilities in graphene and its bilayer, *Phys. Rev. Lett.* 100(1), 016602 (2008)
6. F. Schwierz, Graphene transistors, *Nat. Nanotechnol.* 5(7), 487 (2010)
7. A. Molle, J. Goldberger, M. Houssa, Y. Xu, S. C. Zhang, and D. Akinwande, Buckled two-dimensional xene sheets, *Nat. Mater.* 16(2), 163 (2017)
8. Q. Tang and Z. Zhou, Graphene-analogous low-dimensional materials, *Prog. Mater. Sci.* 58(8), 1244 (2013)
9. K. S. Novoselov, A. Mishchenko, A. Carvalho, and A. H. Castro Neto, 2D materials and van der Waals heterostructures, *Science* 353(6298), aac9439 (2016)
10. S. Lin, J. Gu, Y. Wang, Y. Wang, S. Zhang, X. Liu, H. Zeng, and Z. Chen, Porous silaphosphorene, silaarsenene and silaantimonene: A sweet marriage of Si and P/As/Sb, *J. Mater. Chem. A* 6(8), 3738 (2018)
11. G. Wang, R. Pandey, and S. P. Karna, Atomically thin group V elemental films: theoretical investigations of antimonene allotropes, *ACS Appl. Mater. Interfaces* 7(21), 11490 (2015)
12. L. Kou, C. Chen, and S. C. Smith, Phosphorene: Fabrication, properties, and applications, *J. Phys. Chem. Lett.* 6(14), 2794 (2015)
13. S. Z. Butler, S. M. Hollen, L. Cao, Y. Cui, J. A. Gupta, H. R. Gutierrez, T. F. Heinz, S. S. Hong, J. Huang, A. F. Ismach, E. Johnston-Halperin, M. Kuno, V. V. Plashnitsa, R. D. Robinson, R. S. Ruoff, S. Salahuddin, J. Shan, L. Shi, M. G. Spencer, M. Terrones, W. Windl, and J. E. Goldberger, Progress, challenges, and opportunities in two-dimensional materials beyond graphene, *ACS Nano* 7(4), 2898 (2013)
14. Q. Tang, Z. Zhou, and Z. Chen, Innovation and discovery of graphene-like materials via density-functional theory computations, *Wiley Interdiscip. Rev. Comput. Mol. Sci.* 5(5), 360 (2015)
15. J. J. Zhao, H. S. Liu, Z. M. Yu, R. G. Quhe, S. Zhou, Y. Y. Wang, C. C. Liu, H. X. Zhong, N. N. Han, J. Lu, Y. G. Yao, and K. H. Wu, Rise of silicene: A competitive 2D material, *Prog. Mater. Sci.* 83, 24 (2016)
16. G. G. Guzmán-Verri and L. C. Lew Yan Voon, Electronic structure of silicon-based nanostructures, *Phys. Rev. B* 76(7), 075131 (2007)
17. L. Chen, C. C. Liu, B. Feng, X. He, P. Cheng, Z. Ding, S. Meng, Y. Yao, and K. Wu, Evidence for Dirac fermions in a honeycomb lattice based on silicon, *Phys. Rev. Lett.* 109(5), 056804 (2012)
18. P. De Padova, P. Vogt, A. Resta, J. Avila, I. Razado-Colambo, C. Quaresima, C. Ottaviani, B. Olivieri, T. Bruhn, T. Hirahara, T. Shirai, S. Hasegawa, M. Carmen Asensio, and G. Le Lay, Evidence of Dirac fermions in multilayer silicene, *Appl. Phys. Lett.* 102(16), 163106 (2013)
19. E. Durgun, S. Tongay, and S. Ciraci, Silicon and III-V compound nanotubes: Structural and electronic properties, *Phys. Rev. B* 72(7), 075420 (2005)
20. U. Röthlisberger, W. Andreoni, and M. Parrinello, Structure of nanoscale silicon clusters, *Phys. Rev. Lett.* 72(5), 665 (1994)

21. P. Vogt, P. De Padova, C. Quaresima, J. Avila, E. Frantzeskakis, M. C. Asensio, A. Resta, B. Ealet, and G. Le Lay, Silicene: compelling experimental evidence for graphenelike two-dimensional silicon, *Phys. Rev. Lett.* 108(15), 155501 (2012)

22. S. Cahangirov, M. Topsakal, E. Akturk, H. Sahin, and S. Ciraci, Two- and one-dimensional honeycomb structures of silicon and germanium, *Phys. Rev. Lett.* 102(23), 236804 (2009)

23. K. Takeda and K. Shiraishi, Theoretical possibility of stage corrugation in Si and Ge analogs of graphite, *Phys. Rev. B* 50(20), 14916 (1994)

24. Y. Jing, Z. Zhou, C. R. Cabrera, and Z. F. Chen, Graphene, inorganic graphene analogs and their composites for lithium ion batteries, *J. Mater. Chem. A* 2(31), 12104 (2014)

25. M. Dávila, L. Xian, S. Cahangirov, A. Rubio, and G. Le Lay, Germanene: A novel two-dimensional germanium allotrope akin to graphene and silicene, *New J. Phys.* 16(9), 095002 (2014)

26. M. Houssa, E. Scalise, K. Sankaran, G. Pourtois, V. V. Afanas'ev, and A. Stesmans, Electronic properties of hydrogenated silicene and germanene, *Appl. Phys. Lett.* 98(22), 223107 (2011)

27. L. Li, S. Z. Lu, J. Pan, Z. Qin, Y. Q. Wang, Y. Wang, G. Y. Cao, S. Du, and H. J. Gao, Buckled germanene formation on Pt(111), *Adv. Mater.* 26(28), 4820 (2014)

28. S. Balendhran, S. Walia, H. Nili, S. Sriram, and M. Bhaskaran, Elemental analogues of graphene: Silicene, germanene, stanene, and phosphorene, *Small* 11(6), 640 (2015)

29. F. F. Zhu, W. J. Chen, Y. Xu, C. L. Gao, D. D. Guan, C. H. Liu, D. Qian, S. C. Zhang, and J. F. Jia, Epitaxial growth of two-dimensional stanene, *Nat. Mater.* 14(10), 1020 (2015)

30. P. Z. Tang, P. C. Chen, W. D. Cao, H. Q. Huang, S. Cahangirov, L. D. Xian, Y. Xu, S. C. Zhang, W. H. Duan, and A. Rubio, Stable two-dimensional dumbbell stanene: A quantum spin Hall insulator, *Phys. Rev. B* 90(12), 121408 (2014)

31. S. Rachel and M. Ezawa, Giant magnetoresistance and perfect spin filter in silicene, germanene, and stanene, *Phys. Rev. B* 89(19), 195303 (2014)

32. N. Gao, H. S. Liu, S. Zhou, Y. Z. Bai, and J. J. Zhao, Interaction between post-graphene group-iv honeycomb monolayers and metal substrates: Implication for synthesis and structure control, *J. Phys. Chem. C* 121(9), 5123 (2017)

33. L. Li, Y. Yu, G. J. Ye, Q. Ge, X. Ou, H. Wu, D. Feng, X. H. Chen, and Y. Zhang, Black phosphorus field-effect transistors, *Nat. Nanotechnol.* 9(5), 372 (2014)

34. H. O. Churchill and P. Jarillo-Herrero, Phosphorus joins the family, *Nat. Nanotechnol.* 9(5), 330 (2014)

35. H. Liu, A. T. Neal, Z. Zhu, Z. Luo, X. Xu, D. Tománek, and P. D. Ye, Phosphorene: An unexplored 2D semiconductor with a high hole mobility, *ACS Nano* 8(4), 4033 (2014)

36. A. Carvalho, M. Wang, X. Zhu, A. S. Rodin, H. Su, and A. H. Castro Neto, Phosphorene: From theory to applications, *Nat. Rev. Mater.* 1(11), 16061 (2016)

37. Y. Jing, X. Zhang, and Z. Zhou, Phosphorene: What can we know from computations? *Wiley Interdiscip. Rev. Comput. Mol. Sci.* 6(1), 5 (2016)

38. R. Fei and L. Yang, Strain-engineering the anisotropic electrical conductance of few-layer black phosphorus, *Nano Lett.* 14(5), 2884 (2014)

39. L. Wang, A. Kutana, X. Zou, and B. I. Yakobson, Electro-mechanical anisotropy of phosphorene, *Nanoscale* 7(21), 9746 (2015)

40. H. S. Tsai, S. W. Wang, C. H. Hsiao, C. W. Chen, H. Ouyang, Y. L. Chueh, H. C. Kuo, and J. H. Liang, Direct synthesis and practical bandgap estimation of multilayer arsenene nanoribbons, *Chem. Mater.* 28(2), 425 (2016)

41. S. Zhang, Z. Yan, Y. Li, Z. Chen, and H. Zeng, Atomically thin arsenene and antimonene: Semimetal-semiconductor and indirect-direct band-gap transitions, *Angew. Chem. Int. Ed.* 54(10), 3112 (2015)

42. S. Zhang, S. Guo, Z. Chen, Y. Wang, H. Gao, J. Gómez-Herrero, P. Ares, F. Zamora, Z. Zhu, and H. Zeng, Recent progress in 2D group-VA semiconductors: From theory to experiment, *Chem. Soc. Rev.* 47(3), 982 (2018)

43. S. Zhang, M. Xie, F. Li, Z. Yan, Y. Li, E. Kan, W. Liu, Z. Chen, and H. Zeng, Semiconducting group 15 monolayers: A broad range of band gaps and high carrier mobilities, *Angew. Chem. Int. Ed.* 55(5), 1666 (2016)

44. H. S. Tsai, C. W. Chen, C. H. Hsiao, H. Ouyang, and J. H. Liang, The advent of multilayer antimonene nanoribbons with room temperature orange light emission, *Chem. Commun.* 52(54), 8409 (2016)

45. P. Ares, F. Aguilar-Galindo, D. Rodriguez-San-Miguel, D. A. Aldave, S. Diaz-Tendero, M. Alcami, F. Martin, J. Gomez-Herrero, and F. Zamora, Mechanical isolation of highly stable antimonene under ambient conditions, *Adv. Mater.* 28(30), 6332 (2016)

46. C. Gibaja, D. Rodriguez-San-Miguel, P. Ares, J. Gomez-Herrero, M. Varela, R. Gillen, J. Maultzsch, F. Hauke, A. Hirsch, G. Abellan, and F. Zamora, Few-layer antimonene by liquid-phase exfoliation, *Angew. Chem. Int. Ed.* 55(46), 14345 (2016)

47. J. Ji, X. Song, J. Liu, Z. Yan, C. Huo, S. Zhang, M. Su, L. Liao, W. Wang, Z. Ni, Y. Hao, and H. Zeng, Two-dimensional antimonene single crystals grown by van der Waals epitaxy, *Nat. Commun.* 7, 13352 (2016)

48. J. H. Yuan, N. N. Yu, K. H. Xue, and X. S. Miao, Stability, electronic and thermodynamic properties of aluminene from first-principles calculations, *Appl. Surf. Sci.* 409, 85 (2017)

49. C. Kamal, A. Chakrabarti, and M. Ezawa, Aluminene as highly hole-doped graphene, *New J. Phys.* 17(8), 083014 (2015)

50. D. C. Tyte, $B^2[\pi]$-$A^2[\sigma]$ band system of aluminium monoxide, *Nature* 202(4930), 383 (1964)

51. M. Hoch and H. L. Johnston, Formation, stability and crystal structure of the solid aluminum suboxides: Al_2O and AlO^1, *J. Am. Chem. Soc.* 76(9), 2560 (1954)

52. J. Koput and K. A. Peterson, ab initio prediction of the potential energy surface and vibrational–rotational energy levels of X^2A' BeOH, *J. Phys. Chem. A* 107(19), 3981 (2003)

53. C. Dohmeier, D. Loos, and H. Schnockel, Aluminum(I) and gallium(I) compounds: Syntheses, structures, and reactions, *Angew. Chem. Int. Ed. Engl.* 35(2), 129 (1996)

54. C. Liang, Conduction characteristics of the lithium iodide-aluminum oxide solid electrolytes, *J. Electrochem. Soc.* 120(10), 1289 (1973)

55. S. Zhang, J. Yu, H. Li, D. Mao, and G. Lu, High-effective approach from amino acid esters to chiral amino alcohols over $Cu/ZnO/Al_2O_3$ catalyst and its catalytic reaction mechanism, *Sci. Rep.* 6(1), 33196 (2016)

56. T. T. Song, M. Yang, J. W. Chai, M. Callsen, J. Zhou, T. Yang, Z. Zhang, J. S. Pan, D. Z. Chi, Y. P. Feng, and S. J. Wang, The stability of aluminium oxide monolayer and its interface with two-dimensional materials, *Sci. Rep.* 6(1), 29221 (2016)

57. M. D. Segall, P. J. D. Lindan, M. J. Probert, C. J. Pickard, P. J. Hasnip, S. J. Clark, and M. C. Payne, First-principles simulation: Ideas, illustrations and the CASTEP code, *J. Phys.: Condens. Matter* 14(11), 2717 (2002)

58. M. Kuisma, J. Ojanen, J. Enkovaara, and T. Rantala, Kohn-Sham potential with discontinuity for band gap materials, *Phys. Rev. B* 82(11), 115106 (2010)

59. I. E. Castelli, T. Olsen, S. Datta, D. D. Landis, S. Dahl, K. S. Thygesen, and K. W. Jacobsen, Computational screening of perovskite metal oxides for optimal solar light capture, *Energy Environ. Sci.* 5(2), 5814 (2012)

60. P. Miró, M. Ghorbani-Asl, and T. Heine, Two dimensional materials beyond MoS_2: Noble-transition-metal dichalcogenides, *Angew. Chem. Int. Ed.* 53(11), 3015 (2014)

61. H. Li, C. Tsai, A. L. Koh, L. Cai, A. W. Contryman, A. H. Fragapane, J. Zhao, H. S. Han, H. C. Manoharan, F. Abild-Pedersen, J. K. Nørskov, and X. Zheng, Activating and optimizing MoS_2 basal planes for hydrogen evolution through the formation of strained sulphur vacancies, *Nat. Mater.* 15(1), 48 (2016)

62. Y. Wang, J. Lv, L. Zhu, and Y. Ma, Crystal structure prediction via particle-swarm optimization, *Phys. Rev. B* 82(9), 094116 (2010)

63. K. Takahashi, A. Yoshikawa and A. Sandhu, Wide bandgap Semiconductors, Berlin Heidelberg: Springer-Verlag, 239 (2007)

64. M. N. Yoder, Wide bandgap semiconductor materials and devices, *IEEE Trans. Electron Dev.* 43(10), 1633 (1996)

65. A. Lafond, C. Guillot-Deudon, J. Vidal, M. Paris, C. La, and S. Jobic, Substitution of Li for Cu in Cu_2ZnSnS_4: Toward wide band gap absorbers with low cation disorder for thin film solar cells, *Inorg. Chem.* 56(5), 2712 (2017)

66. T. P. Chow and R. Tyagi, Wide bandgap compound semiconductors for superior high-voltage unipolar power devices, *IEEE Trans. Electron Dev.* 41(8), 1481 (1994)

67. J. Casady and R. W. Johnson, Status of silicon carbide (SiC) as a wide-bandgap semiconductor for high-temperature applications, *Solid State Electron*, 39(10), 1409 (1996)

68. P. G. Neudeck, R. S. Okojie, and L. Y. Chen, High-temperature electronics-a role for wide bandgap semiconductors? *Proc. IEEE* 90(6), 1065 (2002)

69. M. Topsakal, E. Aktürk, and S. Ciraci, First-principles study of two-and one-dimensional honeycomb structures of boron nitride, *Phys. Rev. B* 79(11), 115442 (2009)

70. K. Watanabe, T. Taniguchi, and H. Kanda, Direct-bandgap properties and evidence for ultraviolet lasing of hexagonal boron nitride single crystal, *Nat. Mater.* 3(6), 404 (2004)

71. Y. Kubota, K. Watanabe, O. Tsuda, and T. Taniguchi, Deep ultraviolet light-emitting hexagonal boron nitride synthesized at atmospheric pressure, *Science* 317(5840), 932 (2007)

72. E. Monroy, F. Omnès, and F. Calle, Wide-bandgap semiconductor ultraviolet photodetectors, *Semicond. Sci. Technol.* 18(4), R33 (2003)

73. H. Y. Lu, A. S. Cuamba, L. Geng, L. Hao, Y. M. Qi, and C. Ting, C_3H_2: A wide-band-gap semiconductor with strong optical absorption, *Phys. Rev. B* 96(16), 165420 (2017)